Impurity effect and vortex cluster phase in mesoscopic type-1.5 superconductors

Tian-Yi Han[1], Guo Wang[1], Jie Li[1] and Hai Huang[2⋆]

1 School of Nuclear Science and Engineering, North China Electric Power University, Beijing, 102206, P. R. China
2 Department of Mathematics and Physics, North China Electric Power University, Beijing, 102206, P. R. China

⋆ huanghai@ncepu.edu.cn

Abstract

Based on two-band time-dependent Ginzburg-Landau theory, we study the electromagnetic properties of two-band mesoscopic superconductors. We perform the numerical simulations with the finite element method, and determine the minimum sample size L_c for the existence of the type-1.5 superconductivity from the obtained phase diagram in the absence of impurity. Meanwhile in the presence of an isotropic impurity, our numerical results reveal that the vortex cluster state induced by the attractive defect potential will gradually appear in the mesoscopic system with the sample size $L < L_c$, and the critical defect strength is about 0.2 in the T_c disorder model. In addition, we also investigate the effect of anisotropic defect structures and multiple correlated disorders on the patterns of magnetic vortex distributions. Our theoretical study thus indicates that the diversity of impurity depositions has a significant influence on the semi-Meissner state in mesoscopic type-1.5 superconductors.

Publication information to appear upon publication.

Received Date
Accepted Date
Published Date

Contents

1 Introduction

Over the past two decades, two-band superconductivity has become an important research subject in condensed matter physics. This field started from the discovery of superconductivity in MgB_2 [1], where the existence of two distinct superconducting gaps reveals the complexity of Fermi surface topology in this system. Since then, extensive theoretical and experimental studies have been performed to provide novel insights into unconventional superconducting pairing mechanisms and physical properties in these materials. For example, the multi-gap superconductivity signals a new pathway to achieve more superconducting pairing modes, which can induce phase competition or coexistence between multiple bands by adjusting the external magnetic field or impurity distribution. Furthermore, the magnetic vortex behavior can be optimized through rational design of multi-band structures and its interaction with impurities can improve the overall performance of superconducting devices [2, 3].

As we know, each condensate in two-band superconductors is predicted to support vortex excitation with fractional quantum flux [4]. Due to the interband Josephson coupling, the vortices from different condensates are bounded together with the string interaction and their normal cores will be locked to form a composite vortex with the standard integer quantum flux in the ground state. Recently in a series of experiments of iron-based superconductors, the fractional vortices with a magnitude that varies continuously with temperature have been clearly observed in some special locations [5–7]. In general, the physics of composite vortices in the two-band system will be influenced by the coherence lengths ξ_1 and ξ_2 as well as the magnetic field penetration depth λ. When the particular condition $\xi_1 < \sqrt{2}\lambda < \xi_2$ is satisfied, there may exhibit a new superconducting state that combines characteristics of both type-1 and type-2 superconductors. This so-called semi-Meissner phase or vortex cluster phase is formed due to the interaction of long-range attraction and short-range repulsion between composite vortex excitations [8–10]. The existence of this novel vortex pattern was first visualized by Bitter decorations on high quality MgB_2 single crystal in 2009 [11]. Thereafter, zero-field muon spin experiments have also revealed the presence of this type-1.5 superconducting state in unconventional superconductors Sr_2RuO_4 [12, 13] and $LaPt_3Si$ [14, 15].

In the present paper, we study the electromagnetic effect of type-1.5 superconductors based on the time-dependent Ginzburg-Landau (TDGL) theory. With the COMSOL Multiphysics software and the finite element method, we first obtain the $L-\kappa_1$ phase diagram of the two-band superconductor in the absence of impurity, with L the sample size and κ_1 the GL parameter. Our numerical results demonstrate that there exists a critical sample size L_c for this two-band system, and the semi-Meissner state induced by long-range vortex attraction disappears below L_c. Then in the presence of an isotropic impurity, we show the $g-\kappa_1$ phase diagram with the sample size below L_c, where g represents the disorder strength in this system. For $|g| > 0.22$, we can directly observe the crossover of this mesoscopic system from the diamagnetic Meissner state to the vortex cluster phase, and ultimately to the Abrikosov lattice phase. Furthermore, we also discuss the possible patterns of vortex cluster induced by the anisotropic defect structures and multiple correlated disorders in this superconductor. All of our theoretical results indicate that the diversity of impurity depositions has a significant influence on the collective behaviors of magnetic vortices in the type-1.5 superconducting system.

The rest of this article is organized as follows. In Section 2, we introduce the two-band TDGL theory and apply this formalism to the type-1.5 superconductors. In Section 3, we give the procedure of numerical simulations based on the finite element method. Then in Section 4, we systematically investigate the impurity effect and vortex cluster phase in the mesoscopic system. Finally, Section 5 gives the conclusion of the paper.

2 Model and formalism

The simplest GL free energy functional of two-gap superconductors can be written as [16–20]

$$F = \sum_i \left[\frac{1}{2m_i} \left| \left(-i\hbar\boldsymbol{\nabla} - \frac{2e}{c}\boldsymbol{A} \right) \Psi_i \right|^2 - \alpha_i |\Psi_i|^2 + \frac{\beta_i}{2}|\Psi_i|^4 \right] + \frac{\boldsymbol{B}^2}{8\pi}. \tag{1}$$

Here Ψ_i $(i = 1,2)$ represents the superconducting order parameter and m_i is the effective mass for each band. The coefficient α_i is a function of temperature, while β_i is independent of temperature. $\boldsymbol{B} = \boldsymbol{\nabla} \times \boldsymbol{A}$ is the magnetic induction and $\boldsymbol{A}$ is the vector potential. Starting from the seminal works of Thuneberg [21,22], two main disorder models have been proposed to describe the effect of nonmagnetic impurities on the superconducting system in the framework of the GL theory [23, 24]. The first one is the T_c disorder model with T_c the critical temperature, which is characterized by altering the GL free energy coefficient $\alpha_i \to \alpha_{i0} g(\boldsymbol{r})$ in Eq. (1) [25]. The other one is the l disorder model with l the mean free path, achieved by modifying the effective mass $1/m_i \to (1/m_i)\,h(\boldsymbol{r})$ in Eq. (1), where $h(\boldsymbol{r}) = l/l_m < 1$ represents the ratio of the mean free path inside and outside the well-defined pinning area [26].

If the superconductor is driven out of equilibrium, the order parameter should relax back to its equilibrium value. It is well known that this deviation of superconducting materials can be conveniently described by the TDGL theories. The single-band TDGL equations were first proposed by Schmid [27] and derived from the microscopic BCS theory by Gor'kov and Éliashberg [28]. The extension of TDGL equations to the multi-component superconducting system can be written as [29–32]

$$-\Gamma_i \frac{\partial \Psi_i}{\partial t} = \frac{\delta F}{\delta \Psi_i^*} \quad \text{and} \quad -\sigma_n \frac{\partial \boldsymbol{A}}{\partial t} = \frac{\delta F}{\delta \boldsymbol{A}} \tag{2}$$

where Γ_i is the relaxation time of order parameters and σ_n represents the electrical conductivity of the normal sample in the two-band case. Therefore, minimization of the free energy F with respect to Ψ_i and $\boldsymbol{A}$ leads to the following dimensionless TDGL equations in the zero-electrostatic potential gauge

$$-\Gamma_1 \frac{\partial \Psi_1}{\partial t} = -\left[g(\boldsymbol{r}) - \left|\Psi_1\right|^2 \right] \Psi_1 + h(\boldsymbol{r})(-i\boldsymbol{\nabla} - \boldsymbol{A})^2 \Psi_1, \tag{3}$$

$$-\Gamma_2 \frac{\partial \Psi_2}{\partial t} = -\left[\frac{\alpha_{20}}{\alpha_{10}} g(\boldsymbol{r}) - \frac{\beta_2}{\beta_1} \left|\Psi_2\right|^2 \right] \Psi_2 + \frac{m_1}{m_2} h(\boldsymbol{r})(-i\boldsymbol{\nabla} - \boldsymbol{A})^2 \Psi_2 \tag{4}$$

and

$$-\frac{\partial \boldsymbol{A}}{\partial t} = \kappa_1^2 \boldsymbol{\nabla} \times \boldsymbol{\nabla} \times \boldsymbol{A} - \boldsymbol{J}_s \tag{5}$$

with the supercurrent

$$\boldsymbol{J}_s = h(\boldsymbol{r}) \left\{ \left[\frac{i}{2}(\Psi_1 \nabla \Psi_1^* - \Psi_1^* \nabla \Psi_1) - \left|\Psi_1\right|^2 \boldsymbol{A} \right] + \frac{m_1}{m_2} \left[\frac{i}{2}(\Psi_2 \nabla \Psi_2^* - \Psi_2^* \nabla \Psi_2) - \left|\Psi_2\right|^2 \boldsymbol{A} \right] \right\}. \tag{6}$$

Here in the clean limit with the impurity function $g = h = 1$, we at first introduce the coherence length $\xi_i^2 = \hbar^2/(2m_i\alpha_{i0})$, the London penetration depth $\lambda^{-2} = \lambda_1^{-2} + \lambda_2^{-2}$ with $\lambda_i^{-2} = 4\pi e^2\Psi_{i0}^2/(m_i c^2)$ and $\Psi_{i0} = \sqrt{\alpha_{i0}/\beta_i}$, and the GL parameter $\kappa_1 = \lambda_1/\xi_1$. We then take the coordinate $\boldsymbol{r}$ in units of ξ_1, the time t in units of $t_0 = m_1\sigma_n/\left(4e^2\Psi_{10}^2\right)$, Γ_i in units of $\alpha_{10}t_0$ and the order parameter Ψ_i in units of Ψ_{10}. We also set the magnetic induction $\boldsymbol{B}$ in units of $H_0 = \Phi_0/\left(2\pi\xi_1^2\right)$ with the flux quantum $\Phi_0 = \pi\hbar c/e$ and the vector potential $\boldsymbol{A}$ in units of $A_0 = H_0\xi_1$.

Following Ref. [8], multi-component systems allow a type of superconductivity that is distinct from type-1 or type-2 superconductor. With the condition $\xi_1 < \sqrt{2}\lambda < \xi_2$, the type-1.5 superconducting state will originate from a peculiar vortex interaction which exhibits short-range repulsion and long-range attraction characteristics. The short-range repulsion prevents adjacent vortices from overlapping, while the long-range attraction facilitates the clustering of composite vortices. Consequently, this state is different from type-1 superconductors that completely repel magnetic flux and type-2 superconductors which allow considerable magnetic flux penetration and the formation of vortex lattice. In the ideal sample, the constraint mentioned above can be specifically expressed as

$$\sqrt{\frac{1}{2}\left(1+\frac{m_1}{m_2}\frac{\alpha_{20}}{\alpha_{10}}\frac{\beta_1}{\beta_2}\right)} < \kappa_1 < \sqrt{\frac{1}{2}\left[\frac{m_1}{m_2}\frac{\alpha_{10}}{\alpha_{20}}+\left(\frac{m_1}{m_2}\right)^2\frac{\beta_1}{\beta_2}\right]}. \tag{7}$$

In this circumstance, the magnetic composite vortices will form vortex clusters and coexist with domains of the two-component Meissner state in the framework of the GL theory.

In order to perform systematic numerical simulations, we need to specify appropriate boundary conditions of the superconducting sample. We use the following superconductor-insulator (or vacuum) boundary conditions in the zero-electrostatic potential gauge (see Appendix A for the detailed derivation) [33–35]

$$\boldsymbol{\nabla}\Psi_i\cdot\boldsymbol{n} = 0, \quad \boldsymbol{A}\cdot\boldsymbol{n} = 0 \quad \text{and} \quad \boldsymbol{\nabla}\times\boldsymbol{A} = \boldsymbol{H} \tag{8}$$

where $\boldsymbol{n}$ is the outward unit vector normal to the boundary and the external applied magnetic field is set as $\boldsymbol{H} = H\hat{\boldsymbol{z}}$. The first two conditions just indicate that any current passing through the interface between a superconducting domain and vacuum/insulator would be nonphysical for each band. The third equation represents the continuity of magnetic field across the boundary. The partial differential equations (3)-(5) will be solved numerically for the mesoscopic geometry in the two-dimensional space. The initial conditions at $t = 0$ are taken as $|\Psi_i| = 1$ and $\boldsymbol{A} = (0,0)$ on the xy-plane, corresponding to the Meissner state and zero magnetic field inside the superconductor.

3 Finite element method and numerical computations

Based on the COMSOL Multiphysics software platform [36], we will describe the procedure of the numerical simulations on the TDGL equations in this section. We first split the order parameters into the real and imaginary parts, i.e. $\Psi_1 = u_1 + iu_2$ and $\Psi_2 = u_3 + iu_4$. The magnetic potential is also written in component form as $\boldsymbol{A} = (u_5, u_6)$. In order to implement the boundary conditions, we will introduce an auxiliary variable $u_7(x,y,t)$ for reasons explained below. In the procedure of simulations, we set $\Gamma_1 = \Gamma_2 = 5$ and $m_1 = 2m_2$. To stabilize the semi-Meissner state, we also take $\alpha_{10} = \alpha_{20}$ and $\beta_1 = \beta_2$ in the calculations.

In this way, we can transform the TDGL equations into the general form of partial differential equations in this software package

$$\sum_k \mu_{jk}\frac{\partial u_k}{\partial t}+\sum_l \partial_l \nu_{jl}=\eta_j. \tag{9}$$

Here we have $j,k=1,2,\cdots,7$, $l=1,2$ and $(\partial_1,\partial_2)=(\partial_x,\partial_y)$. The 7×7 matrix μ_{jk} and the 7×2 column vector ν_{jl} take the form

$$\mu_{jk}=\begin{bmatrix} 5 & 0 & 0 & 0 & 0 & 0 & 0\\ 0 & 5 & 0 & 0 & 0 & 0 & 0\\ 0 & 0 & 5 & 0 & 0 & 0 & 0\\ 0 & 0 & 0 & 5 & 0 & 0 & 0\\ 0 & 0 & 0 & 0 & 1 & 0 & 0\\ 0 & 0 & 0 & 0 & 0 & 1 & 0\\ 0 & 0 & 0 & 0 & 0 & 0 & 0 \end{bmatrix} \tag{10}$$

and

$$\nu_{jl}=\begin{bmatrix} -h(\boldsymbol{r})u_{1x} & -h(\boldsymbol{r})u_{1y}\\ -h(\boldsymbol{r})u_{2x} & -h(\boldsymbol{r})u_{2y}\\ -2h(\boldsymbol{r})u_{3x} & -2h(\boldsymbol{r})u_{3y}\\ -2h(\boldsymbol{r})u_{4x} & -2h(\boldsymbol{r})u_{4y}\\ 0 & \kappa_1^2\left(u_{6x}-u_{5y}-H\right)\\ \kappa_1^2\left(u_{5y}-u_{6x}+H\right) & 0\\ u_5 & u_6 \end{bmatrix}. \tag{11}$$

Noting that the subscript x or y denotes the partial derivative with respect to the corresponding variable here. Meanwhile, the driving force η_j contains all other terms in the TDGL equations except the left handed side of Eq. (9), and detailed calculations will give all the components explicitly as

$$\eta_1=\left[g(\boldsymbol{r})-\left(u_1^2+u_2^2\right)\right]u_1-h(\boldsymbol{r})\left[\left(u_5^2+u_6^2\right)u_1-\left(u_{5x}+u_{6y}\right)u_2-2\left(u_{2x}u_5+u_{2y}u_6\right)\right], \tag{12}$$

$$\eta_2=\left[g(\boldsymbol{r})-\left(u_1^2+u_2^2\right)\right]u_2-h(\boldsymbol{r})\left[\left(u_5^2+u_6^2\right)u_2+\left(u_{5x}+u_{6y}\right)u_1+2\left(u_{1x}u_5+u_{1y}u_6\right)\right], \tag{13}$$

$$\eta_3=\left[g(\boldsymbol{r})-\left(u_3^2+u_4^2\right)\right]u_3-2h(\boldsymbol{r})\left[\left(u_5^2+u_6^2\right)u_3-\left(u_{5x}+u_{6y}\right)u_4-2\left(u_{4x}u_5+u_{4y}u_6\right)\right], \tag{14}$$

$$\eta_4=\left[g(\boldsymbol{r})-\left(u_3^2+u_4^2\right)\right]u_4-2h(\boldsymbol{r})\left[\left(u_5^2+u_6^2\right)u_4+\left(u_{5x}+u_{6y}\right)u_3+2\left(u_{3x}u_5+u_{3y}u_6\right)\right], \tag{15}$$

$$\eta_5=h(\boldsymbol{r})\left[\left(u_{2x}u_1-u_{1x}u_2\right)+2\left(u_{4x}u_3-u_{3x}u_4\right)-\left(u_1^2+u_2^2+2u_3^2+2u_4^2\right)u_5\right], \tag{16}$$

$$\eta_6=h(\boldsymbol{r})\left[\left(u_{2y}u_1-u_{1y}u_2\right)+2\left(u_{4y}u_3-u_{3y}u_4\right)-\left(u_1^2+u_2^2+2u_3^2+2u_4^2\right)u_6\right], \tag{17}$$

$$\eta_7=u_{5x}+u_{6y}+u_7. \tag{18}$$

Now we can examine the boundary conditions in this formalism. With the normal vector $\boldsymbol{n}=(n_1,n_2)$ and the column vector ν_{jl}, the boundary conditions in Eq. (8) can be simply casted into the compact form as

$$\sum_l n_l v_{jl} = 0 \tag{19}$$

which is best suited to the COMSOL Multiphysics simulations. We also note that from the last equation ($j = 7$) in (9), our manipulations will give a trivial solution $u_7 = 0$ for this auxiliary variable and it insures the self-consistency of our problem.

COMSOL Multiphysics is a simulation platform based on the finite element method widely employed in solving coupled physical problems in engineering and fundamental research. The software numerically resolves partial differential equations by discretizing the continuous computational domain into a mesh composed of finite elements [37–39]. In two-dimensional geometries, triangular elements are generally adopted due to their adaptability to irregular boundaries and complex shapes. Based on this discretization, a local function space is constructed to approximate the field variables, typically using piecewise polynomial basis functions to maintain the continuity and stability across element interfaces [40]. To handle time-dependent problems with high accuracy and robustness, COMSOL utilizes implicit time-stepping schemes and often incorporates stable integration methods such as the backward Euler formulation. In our numerical calculations, we take the time step $\Delta t = 0.5t_0$ and treat a simulation as converged when the relative variations of the order parameter $|\Psi_1|$ between two sequential steps are smaller than 10^{-8}. We also set the snapshot time at $t = 10^4 t_0$, which will be justified from two perspectives in Appendix B.

4 Results and discussions

In this section, we will set the external magnetic field $H = 0.8H_0$ and systematically explore the effects of sample boundary and impurities on various vortex excitations. Based on the TDGL theory (3)-(5), we first perform the numerical calculations to obtain the $L - \kappa_1$ and $g - \kappa_1$ phase diagrams in the two-band superconductor. Then, we investigate the effect of anisotropic defect structures and multiple correlated disorders on the patterns of magnetic vortex distributions in the mesoscopic sample.

Before the detailed numerical simulations, we would like to briefly discuss the method of determining the critical points of the phase transitions in the two-gap superconducting system. Following Ref. [41], we can identify the phase separation lines in $L - \kappa_1$ and $g - \kappa_1$ phase diagrams from the dependence of magnetization M on the GL parameter κ_1 in our investigations. For the type-2 superconductor, at small κ_1 the system will stay at the Meissner phase and give the magnetization $-4\pi M = H - \langle B\rangle \approx 0.8H_0$ due to the perfect diamagnetism, where $\langle B\rangle = \langle u_{6x} - u_{5y}\rangle$ describes the average magnetic induction over the sample area S. While at large κ_1, the magnetic field penetrates the superconductor to form the Abrikosov vortex lattice and the magnetization will reduce gradually in a broad range of κ_1. Thus, with the definition of $M' = \mathrm{d}M/\mathrm{d}\kappa_1$, it will show a discontinuous jump at the critical κ_1 of the phase transition from the perfect diamagnetic state to the vortex lattice state. For the type-1.5 superconductor, at small κ_1 the sample remains in the Meissner state and M is still close to $0.8H_0$. With the increase of κ_1, the system first enters the vortex cluster phase and the magnetization will decrease linearly in a narrow range of κ_1 exactly as in the case of the intermediate state of type-1 superconductors. As κ_1 is further raised, we will observe the vortex lattice phase, and the decline in M will exhibit a significant deceleration compared to the vortex cluster phase due to the dominance of short-range repulsive intervortex interaction. In this circumstance, M' will display two discontinuous jumps at the critical points of the phase transitions from the perfect diamagnetic state to the vortex cluster state, and ultimately to the vortex lattice state. We note that the identification method discussed above is still applicable to systems with a relatively small number of vortices.

4.1 $L-\kappa_1$ phase diagram in the clean limit

In this subsection, we first investigate the $L-\kappa_1$ phase diagram of the $L\times L$ two-band superconductor in the absence of impurity. As an example, we choose $15\xi_1\times 15\xi_1$ and $50\xi_1\times 50\xi_1$ superconducting samples to determine the critical κ_1 in the phase transitions. We then plot the variations of M and its derivative with κ_1 at $t=10^4 t_0$ in Fig. 1. From Fig. 1, we can observe that the $15\xi_1\times 15\xi_1$ system exhibits the type-2 magnetic behavior. At small κ_1, the superconductor stays at the Meissner phase and the perfect diamagnetism leads to $-4\pi M\approx 0.8H_0$. While at large κ_1, the sample enters the vortex lattice phase and M reduces gradually in a broad range of κ_1. On the contrary, we can also see from Fig. 1 that the $50\xi_1\times 50\xi_1$ system shows the type-1.5 superconducting properties. At small κ_1, the superconductor remains at the Meissner state and M is still close to $0.8H_0$. With the increase of κ_1, the magnetic field starts to penetrate the sample and the flux lines will exist in the form of the magnetic cluster due to the long-range attractive interaction between vortices, which induces a linear decrease of the magnetization in a narrow range of κ_1. As κ_1 is further raised, the number of vortices in the system continues to increase and eventually forms the stable Abrikosov flux lattice. In this circumstance, the rate of increase in vortex density will significantly slow down compared to the vortex cluster phase due to the dominance of short-range repulsive intervortex interaction. In order to accurately determine the critical points of the phase transitions, we further calculate the first-order derivative M' as a function of κ_1 in the inset of Fig. 1. It can be clearly observed that for the $15\xi_1\times 15\xi_1$ superconductor, M' exhibits a discontinuous jump at $\kappa_1=1.48$, which denotes the transition of the system from the Meissner state to the vortex lattice state. For the $50\xi_1\times 50\xi_1$ superconductor, M' shows two discontinuous jumps and the sample enters the vortex cluster phase at $\kappa_1=1.28$, then transfers to the vortex lattice phase at $\kappa_1=1.67$.

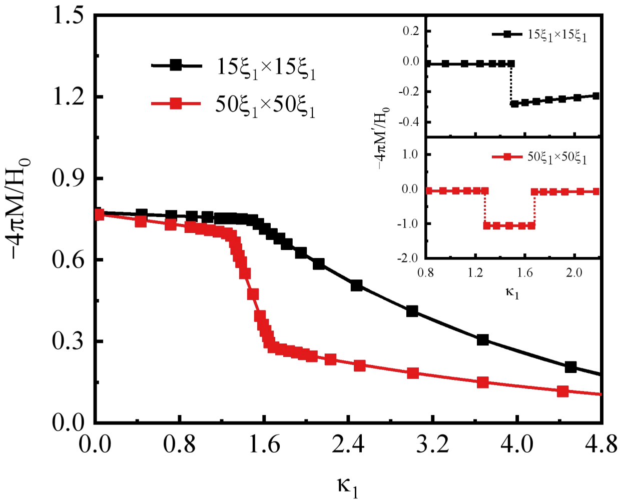

Figure 1: Variations of magnetization M (main) and its first-order derivative M' (inset) with GL parameter κ_1 for the $L\times L$ two-band superconductor in the absence of impurity. We set the external magnetic field $H=0.8H_0$ in the numerical simulations.

With this approach, we can further calculate the critical κ_1 for arbitrary value of L and obtain the $L-\kappa_1$ phase diagram as shown in Fig. 2. It can be seen from Fig. 2 that with the decrease of L, the vortex cluster phase produced by the long-range attractive interaction between vortices gradually vanishes. Meanwhile, we also notice the critical sample size L_c for the disappearance of this cluster state is $32\xi_1$. Thus, the superconducting system will stay in the type-1.5 regime above L_c and the type-2 regime below L_c in the absence of impurity.

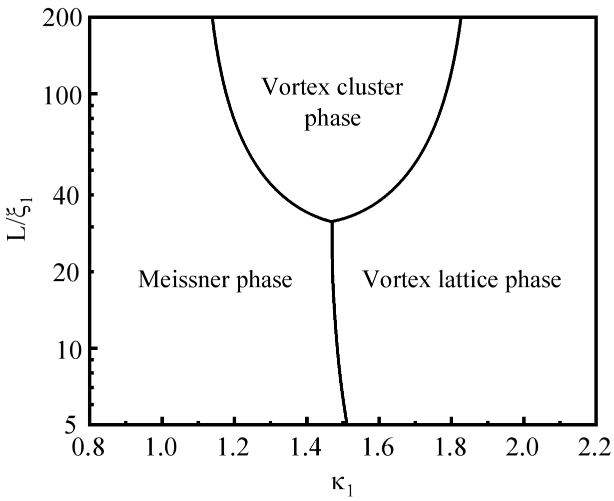

Figure 2: The $L-\kappa_1$ phase diagram of the $L\times L$ two-band superconductor in the absence of impurity. We set the external magnetic field $H=0.8H_0$ in the numerical simulations, and plot the sample size L on a logarithmic scale.

As we know, the type-1.5 superconductor originates from a peculiar vortex interaction that exhibits short-range repulsion and long-range attraction characteristics. The obtained critical L_c is consistent with the characteristic length scale (about 30ξ) of the crossover from the attractive to repulsive intervortex interaction [9]. For the sample size $L>L_c$, the long-range attractive potential between vortices will dominate at the external magnetic field $H=0.8H_0$ and the system is allowed to spontaneously form the stable vortex cluster. However for $L<L_c$, the repulsive intervortex interaction will prevail in the mesoscopic superconductor and the vortex cluster phase can only be induced by other effects such as impurities.

In addition to the superconducting square discussed above, we further examine the transition behaviors of mesoscopic samples with the aspect ratio different from 1 in the absence of impurity. As a simple example, we choose the $15\xi_1\times 20\xi_1$ superconducting sample with each side length below L_c. We plot the magnetic induction $B=u_{6x}-u_{5y}$ in units of H_0 and the order parameter of the first condensate $\left|\Psi_1\right|=\sqrt{u_1^2+u_2^2}$ in units of Ψ_{10} at $t=10^4t_0$ in Fig. 3. With the increase of the GL parameter κ_1, we can see the direct transition of this system from the perfect diamagnetic state to the Abrikosov lattice phase as shown in Fig. 3. All of these numerical results thus suggest that the vortex cluster phase will be excluded for arbitrary mesoscopic sample with the characteristic scale less than L_c in the absence of impurity.

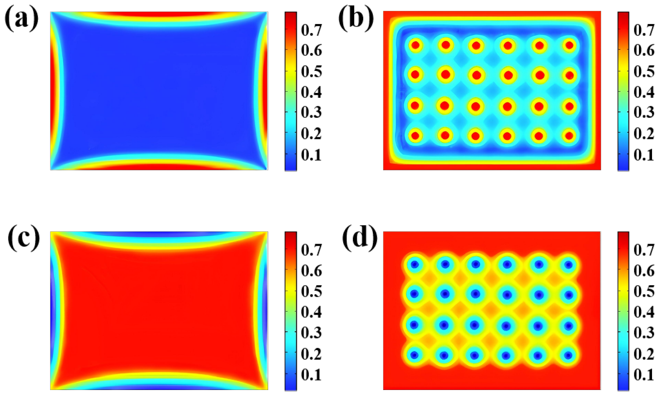

Figure 3: Transition of the magnetic induction B (a,b) and the order parameter of the first condensate $\left|\Psi_1\right|$ (c,d) for the $15\xi_1 \times 20\xi_1$ type-2 superconductor. The snapshots show the Meissner phase (a,c) and vortex lattice phase (b,d) at the GL parameter $\kappa_1 = 0.70$ and 2.10 respectively. The magnetization only has the component perpendicular to the superconducting plane.

4.2 Effect of an isotropic impurity in the T_c and l disorder models

Now, we try to explore the possible generation of the vortex cluster phase in the mesoscopic superconducting system with $L < L_c$ due to the impurity effect. As an example, we introduce an isotropic impurity with the radius $0.5\xi_1$ at the center of the $15\xi_1 \times 15\xi_1$ superconducting sample here. With the T_c disorder model, the defect function $g(\boldsymbol{r})$ will be characterized by the disorder strength g inside the impurity and $h(\boldsymbol{r}) = 1$. We set the value of g as -0.1 and -0.5, and then plot the variations of M and its derivative with κ_1 at $t = 10^4 t_0$ in Fig. 4. From Fig. 4, we can observe that for $g = -0.1$, this mesoscopic system exhibits the type-2 magnetic behavior. With the transition of the superconductor from the Meissner state to the vortex lattice state, the magnetization reduces gradually from the perfect diamagnetism $-4\pi M \approx 0.8H_0$. Meanwhile, we can also see from Fig. 4 that for $g = -0.5$, the sample shows the type-1.5 superconducting properties. In the process of the transitions from the perfect diamagnetic state to the vortex cluster state, and ultimately to the vortex lattice state, the magnetization curve first remains close to $0.8H_0$, then decreases linearly in a narrow range of κ_1 and finally reduces with a relatively small extent compared to its neighboring phase. Furthermore, we can clearly observe from the inset of Fig. 4 that for $g = -0.1$, the phase transition from the Meissner state directly to the vortex lattice state appears at $\kappa_1 = 1.38$. For $g = -0.5$, the magnetic flux lines in this mesoscopic superconductor condense into the vortex cluster at $\kappa_1 = 1.08$ and further form the Abrikosov vortex lattice at $\kappa_1 = 1.58$.

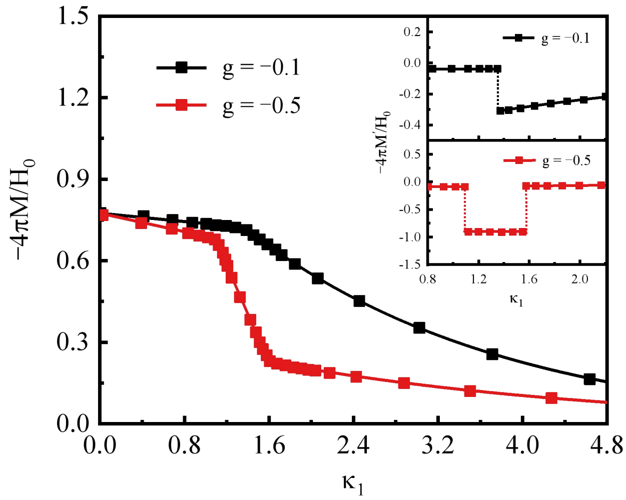

Figure 4: Variations of magnetization M (main) and its first-order derivative M' (inset) with GL parameter κ_1 for the $15\xi_1 \times 15\xi_1$ two-band superconductor in the presence of an isotropic impurity. We set the external magnetic field $H = 0.8H_0$ in the numerical simulations.

With this approach, we can calculate the critical κ_1 for arbitrary value of g and obtain the $g - \kappa_1$ phase diagram as shown in Fig. 5. It can be seen from Fig. 5 that with the increase of the absolute value of g, the vortex cluster phase induced by the attractive interaction from the impurity will gradually appear in the system. Meanwhile, we also see that there exists a critical impurity strength $g_c \approx -0.22$ for the generation of the vortex cluster state in this sample. Thus, the $15\xi_1 \times 15\xi_1$ mesoscopic superconductor will stay in the type-1.5 regime for $|g| > |g_c|$ in the presence of an isotropic impurity. Furthermore, it is clearly observed that for $|g| > |g_c|$, with the increase of $|g|$ the system transfers from the Meissner phase to the vortex cluster phase at a smaller critical κ_1, and then enters the vortex lattice phase at a larger κ_1 value.

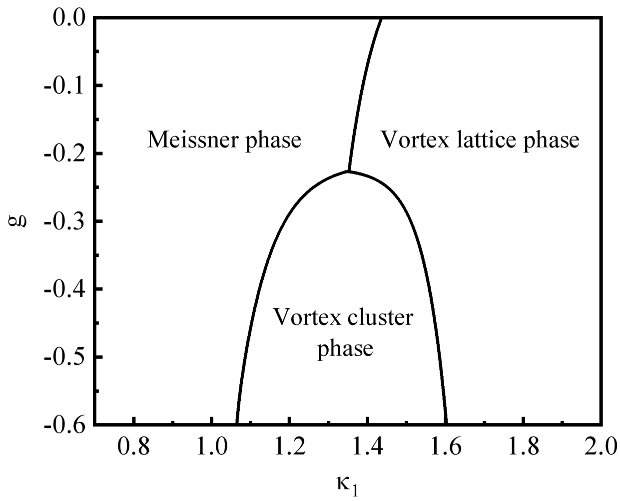

Figure 5: The $g - \kappa_1$ phase diagram of the $15\xi_1 \times 15\xi_1$ two-band superconductor in the presence of an isotropic impurity. We set the external magnetic field $H = 0.8H_0$ in the numerical simulations.

At this point, in order to demonstrate the robustness of vortex cluster phase induced by the localized impurity in the type-1.5 superconductor, we compare the numerical results computed from two types of disorder models, i.e., the T_c disorder model and the l disorder model. For the T_c disorder model, we choose the impurity function g to take the phenomenological form [25]

$$g(\boldsymbol{r}) = \begin{cases} -0.5, & \text{if } |\boldsymbol{r} - \boldsymbol{r}_0| < 0.5\xi_1 \\ 1\,, & \text{otherwise} \end{cases} \tag{20}$$

with $|g| > |g_c|$ inside the impurity. It is easy to see that this circular defect is centered at $\boldsymbol{r}_0 = (x_0, y_0)$. For simplicity, we insert this pinning site at the center of the $15\xi_1 \times 15\xi_1$ superconducting square. We plot the magnetic induction B and the order parameter of the first condensate $|\Psi_1|$ at $t = 10^4 t_0$ in Fig. 6. With the GL parameter κ_1 taken as 0.70, 1.30 and 2.10 sequentially, we can clearly observe the transitions of this type-1.5 system from the perfect diamagnetism state to the vortex cluster phase, and ultimately to the Abrikosov lattice phase. Our numerical simulations also show that the cluster phase presents the vortex pattern with octagonal symmetry and appears in the region of $1.08 < \kappa_1 < 1.58$. Moreover, it can be seen from Fig. 6(c,f) that the isotropic defect induces the localized distortion of the Abrikosov flux lattice, but will still preserve the C_4 rotational symmetry of the superconducting system.

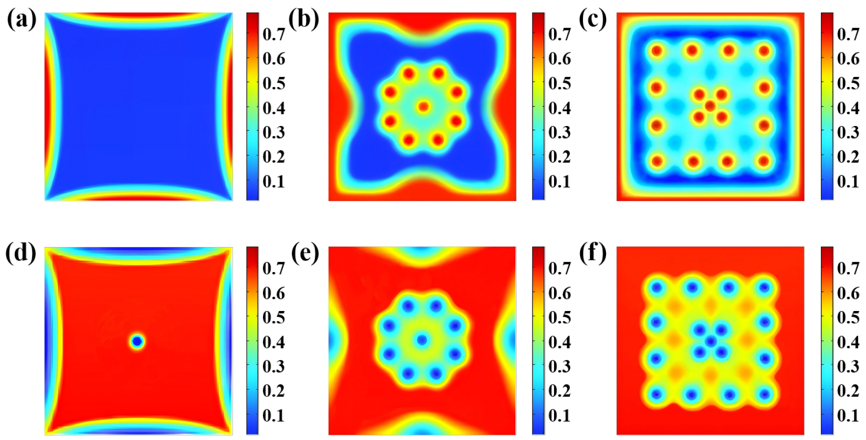

Figure 6: Transitions of the magnetic induction B (a-c) and the order parameter of the first condensate $|\Psi_1|$ (d-f) for the T_c disorder model at the presence of an isotropic defect in the $15\xi_1 \times 15\xi_1$ type-1.5 superconductor. The snapshots show the Meissner phase (a,d), vortex cluster phase (b,e) and vortex lattice phase (c,f) at the GL parameter $\kappa_1 = 0.70$, 1.30 and 2.10 respectively. The magnetization only has the component perpendicular to the superconducting plane.

For the l disorder model, we set $g(\boldsymbol{r}) = 1$ and the impurity function h as [26]

$$h(\boldsymbol{r}) = \begin{cases} 0.2, & \text{if } |\boldsymbol{r} - \boldsymbol{r}_0| < 0.5\xi_1 \\ 1\,, & \text{otherwise} \end{cases} \tag{21}$$

with $h < h_c$ inside the impurity. Here h_c stands for the critical disorder strength for the formation of the vortex cluster state in the l disorder model, which is estimated as 0.6 from our numerical simulations. Then, we also insert this pinning site at the center of the $15\xi_1 \times 15\xi_1$ mesoscopic sample. The magnetic induction B and the order parameter of the first condensate $|\Psi_1|$ at $t = 10^4 t_0$ are plotted in Fig. 7. For the GL parameter $\kappa_1 = 1.30$ and 2.10, we can observe a vortex cluster pattern with octagonal symmetry in Fig. 7(b,e) and the locally distorted flux lattice with C_4 rotational symmetry in Fig. 7(c,f) respectively. For this particular disorder model, the vortex cluster phase is generated around the pinning site within the range $1.06 < \kappa_1 < 1.59$. Based on the numerical results mentioned above, we can conclude that within the framework of the GL theory, the T_c and l disorder models are qualitatively equivalent in describing the local effect of the impurity on collective vortex distributions for the type-1.5 superconductor.

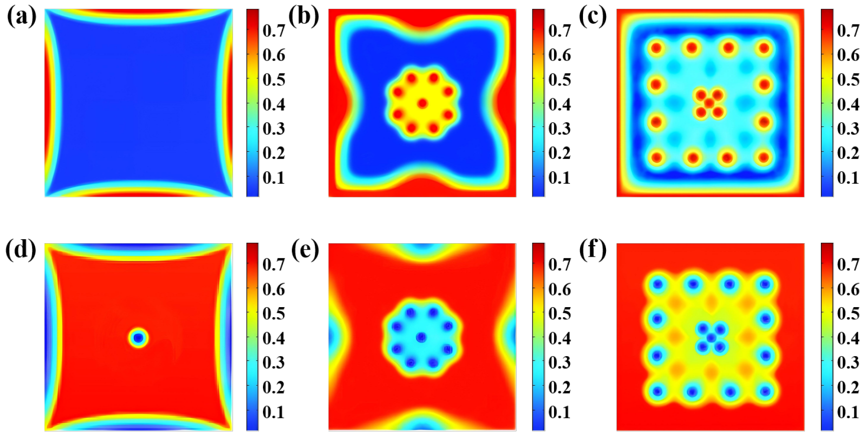

Figure 7: Transitions of the magnetic induction B (a-c) and the order parameter of the first condensate $|\Psi_1|$ (d-f) for the l disorder model at the presence of an isotropic defect in the $15\xi_1 \times 15\xi_1$ type-1.5 superconductor. The snapshots show the Meissner phase (a,d), vortex cluster phase (b,e) and vortex lattice phase (c,f) at the GL parameter $\kappa_1 = 0.70$, 1.30 and 2.10 respectively. The magnetization only has the component perpendicular to the superconducting plane.

At the same time, in the type-2 regime, we take the defect strength $g = -0.1$ for the T_c disorder model and $h = 0.8$ for the l disorder model inside each isotropic impurity. We still insert this pinning site at the center of the $15\xi_1 \times 15\xi_1$ superconducting square. We plot the magnetic induction B and the order parameter of the first condensate $|\Psi_1|$ at $t = 10^4 t_0$ in Fig. 8 and Fig. 9. With the GL parameter κ_1 taken as 0.70 and 2.10 sequentially, we can observe the direct transition of this type-2 system from the perfect diamagnetic state to the Abrikosov lattice phase in Fig. 8 and Fig. 9. Based on the numerical calculations mentioned above, we can see that both the T_c and l disorder models give the similar results for the type-2 systems.

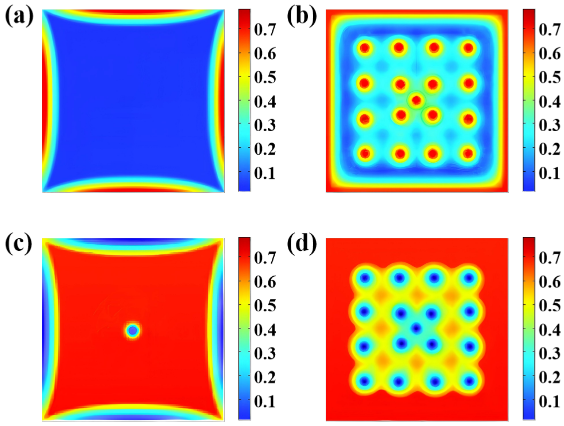

Figure 8: Transition of the magnetic induction B (a,b) and the order parameter of the first condensate $|\Psi_1|$ (c,d) for the T_c disorder model at the presence of an isotropic defect in the $15\xi_1 \times 15\xi_1$ type-2 superconductor. The snapshots show the Meissner phase (a,c) and vortex lattice phase (b,d) at the GL parameter $\kappa_1 = 0.70$ and 2.10 respectively. The magnetization only has the component perpendicular to the superconducting plane.

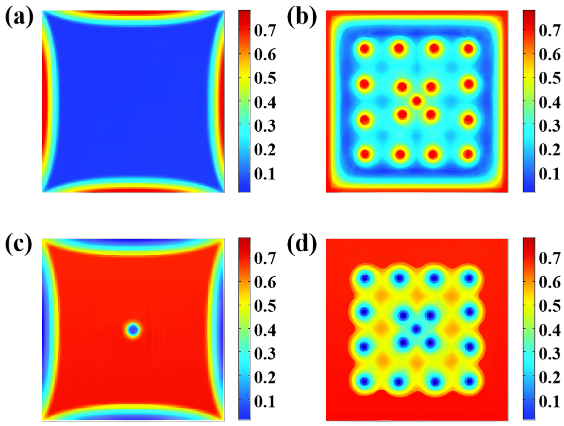

Figure 9: Transition of the magnetic induction B (a,b) and the order parameter of the first condensate $|\Psi_1|$ (c,d) for the l disorder model at the presence of an isotropic defect in the $15\xi_1 \times 15\xi_1$ type-2 superconductor. The snapshots show the Meissner phase (a,c) and vortex lattice phase (b,d) at the GL parameter $\kappa_1 = 0.70$ and 2.10 respectively. The magnetization only has the component perpendicular to the superconducting plane.

4.3 Vortex cluster phase in the presence of an anisotropic impurity

In addition to the isotropic impurity discussed above, we will investigate the effect of triangular and square defect configurations on the vortex cluster phase in the T_c disorder model. The triangular or square impurity is with a side length of ξ_1 and placed at the center of the $15\xi_1 \times 15\xi_1$ mesoscopic superconducting system. We also set the impurity function $g = -0.5$ inside the impurity. Then, we plot the magnetic induction B and the order parameter of the first condensate $|\Psi_1|$ at $t = 10^4 t_0$ for triangular and square defect configurations in Fig. 10 and Fig. 11 respectively. With the GL parameter κ_1 taken as 0.70, 1.30 and 2.10 sequentially, we can clearly observe the transitions of this system from the perfect diamagnetism state to the vortex cluster phase, and ultimately to the vortex lattice phase. For the triangular (or square) impurity case, the peculiar vortex cluster is generated around the pinning site within the range $1.15 < \kappa_1 < 1.52$ (or $1.03 < \kappa_1 < 1.62$). It can be seen from Fig. 10(b,e) that the introduction of triangular defect breaks the C_4 rotational symmetry of the mesoscopic system and will form a distorted cluster in this circumstance. In contrast, the presence of square impurity ensures that the vortex pattern will still preserve the C_4 rotational symmetry, as shown in Figs. 11(b,e) and 11(c,f).

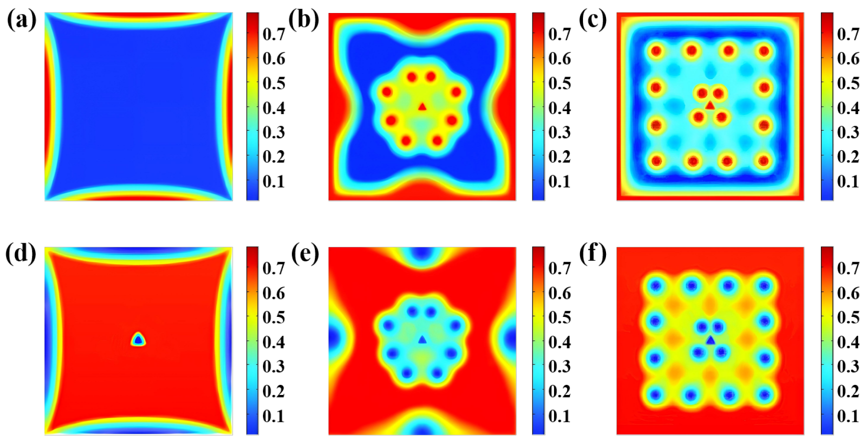

Figure 10: Transitions of the magnetic induction B (a-c) and the order parameter of the first condensate $|\Psi_1|$ (d-f) at the presence of a triangular defect in the $15\xi_1 \times 15\xi_1$ type-1.5 superconductor. The snapshots show the Meissner phase (a,d), vortex cluster phase (b,e) and vortex lattice phase (c,f) at the GL parameter $\kappa_1 = 0.70$, 1.30 and 2.10 respectively. The magnetization only has the component perpendicular to the superconducting plane.

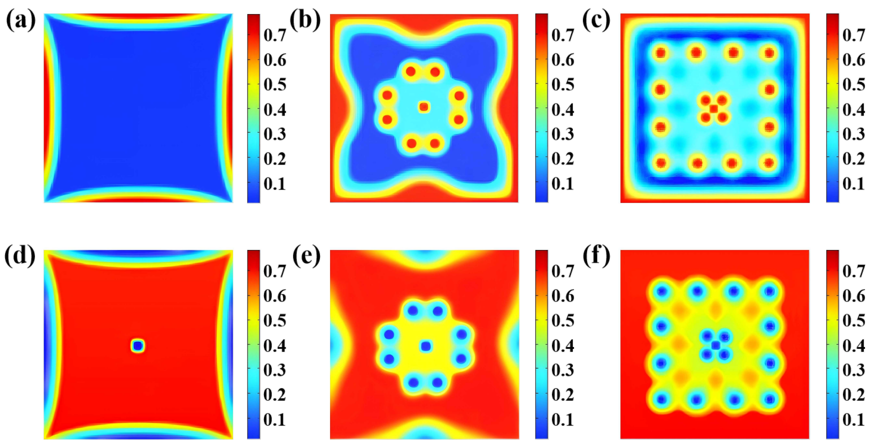

Figure 11: Transitions of the magnetic induction B (a-c) and the order parameter of the first condensate $|\Psi_1|$ (d-f) at the presence of a square defect in the $15\xi_1 \times 15\xi_1$ type-1.5 superconductor. The snapshots show the Meissner phase (a,d), vortex cluster phase (b,e) and vortex lattice phase (c,f) at the GL parameter $\kappa_1 = 0.70$, 1.30 and 2.10 respectively. The magnetization only has the component perpendicular to the superconducting plane.

4.4 Uncorrelated and correlated disorder systems

In this subsection, we set the disorder strength $|g| > |g_c|$ at the impurity sites in the T_c disorder model, and discuss the effects of multiple uncorrelated and correlated defects on vortex cluster patterns in the $15\xi_1 \times 15\xi_1$ mesoscopic superconductor. In the uncorrelated case, we choose the impurity function $g(\boldsymbol{r})$ to take the phenomenological form

$$g(\boldsymbol{r}) = \prod_{n=1}^{N} g_n(\boldsymbol{r}) \quad \text{with} \quad g_n(\boldsymbol{r}) = \begin{cases} -0.5, & \text{if } |\boldsymbol{r} - \boldsymbol{r}_{0n}| < 0.5\xi_1 \\ 1\,, & \text{otherwise} \end{cases} . \tag{22}$$

It is easy to see that the isotropic impurity is centered at $\boldsymbol{r}_{0n} = (x_{0n}, y_{0n})$ with $n = 1, 2, ..., N$. For simplicity, we take the impurity number $N = 2$ and select the pinning centers at $(\pm 3\xi_1, 0)$ in $15\xi_1 \times 15\xi_1$ superconducting sample, which ensures the uncorrelation between these two defects. We plot the magnetic induction B and the order parameter of the first condensate $|\Psi_1|$ at $t = 10^4 t_0$ in Fig. 12. Different from the single impurity case, multiple vortex clusters are generated around the pinning sites within $0.87 < \kappa_1 < 1.77$. With the GL parameter $\kappa_1 = 1.30$, we can see from Fig. 12(b,e) that each vortex cluster exhibits the identical pattern with hexagonal symmetry. Meanwhile for $\kappa_1 = 2.10$, as shown in Fig. 12(c,f), we can clearly observe the localized distortions around the pinning positions in the flux lattice due to the attraction of vortices by impurities.

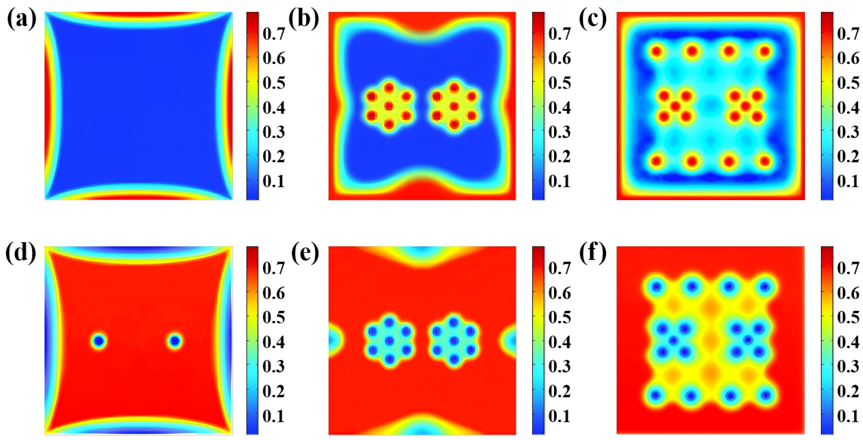

Figure 12: Transitions of the magnetic induction B (a-c) and the order parameter of the first condensate $|\Psi_1|$ (d-f) at the presence of two uncorrelated defects in the $15\xi_1 \times 15\xi_1$ type-1.5 superconductor. The snapshots show the Meissner phase (a,d), vortex cluster phase (b,e) and vortex lattice phase (c,f) at the GL parameter $\kappa_1 = 0.70$, 1.30 and 2.10 respectively. The magnetization only has the component perpendicular to the superconducting plane.

In order to take into account the spatial correlation between these impurities, we choose the following continuous pinning function [42, 43]

$$g(\boldsymbol{r}) = \prod_{n=1}^{N} g_n(\boldsymbol{r}) \quad \text{with} \quad g_n(\boldsymbol{r}) = \tanh\left(\frac{|\boldsymbol{r} - \boldsymbol{r}_{0n}| - R}{R_0}\right). \tag{23}$$

We take $R = 0.5\xi_1$ and $R_0 = 1.5\xi_1$ in Eq. (23), and then perform numerical simulations in the $15\xi_1 \times 15\xi_1$ mesoscopic superconductor. For comparison with the uncorrelated case, we still choose the defect centers at $(\pm 3\xi_1, 0)$. We plot the magnetic induction B and the order parameter of the first condensate $|\Psi_1|$ at $t = 10^4 t_0$ in Fig. 13. Note that with this new impurity function, we can obtain the stable vortex cluster phase within $0.92 < \kappa_1 < 1.71$. For $\kappa_1 = 1.30$, it is shown in Fig. 13(b,e) that two vortex clusters induced by uncorrelated disorders in Fig. 12(b,e) are fused into a single larger cluster here. Meanwhile with $\kappa_1 = 2.10$, we can find a vortex lattice pattern with local distortions around the impurities in Fig. 13(c,f).

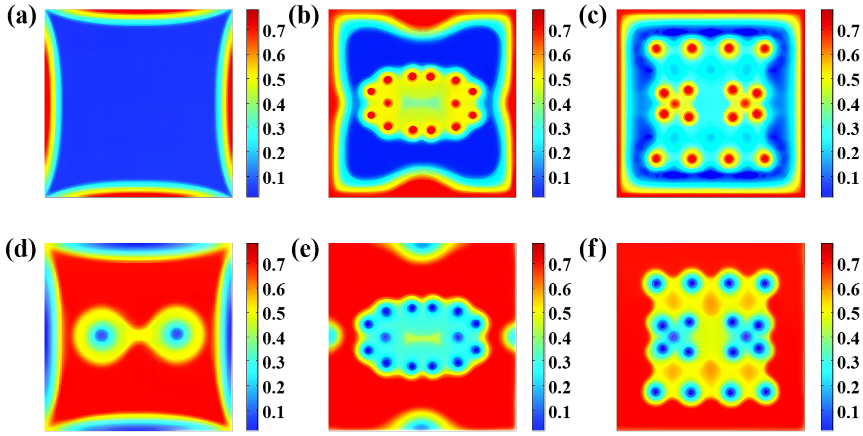

Figure 13: Transitions of the magnetic induction B (a-c) and the order parameter of the first condensate $|\Psi_1|$ (d-f) at the presence of two correlated defects in the $15\xi_1 \times 15\xi_1$ type-1.5 superconductor. The snapshots show the Meissner phase (a,d), vortex cluster phase (b,e) and vortex lattice phase (c,f) at the GL parameter $\kappa_1 = 0.70$, 1.30 and 2.10 respectively. The magnetization only has the component perpendicular to the superconducting plane.

5 Conclusion

Based on two-band TDGL theory, we explore the impurity effect on the vortex collective behaviors in the mesoscopic type-1.5 superconductor. With the finite element method, the investigations suggest that the vortex cluster phase will be excluded for arbitrary mesoscopic sample with the characteristic scale less than L_c in the absence of impurity. In the presence of an isotropic impurity, our numerical results give the direct evidence for the existence of semi-Meissner state at $|g| > |g_c|$ due to the attractive defect interaction. We also discuss the effect of anisotropic defect structures and multiple correlated disorders on the possible patterns of magnetic vortex distributions. We hope that our theoretical results will inspire further research on better understanding novel vortex dynamics and transport properties in two-band superconductors.

Acknowledgements

One of the authors (H.H.) would like to thank Prof. Z.-Z. Gan for helpful discussions. We would also like to thank the anonymous referees for very inspiring suggestions.

Author contributions Conceptualization, T.H., G.W., J.L. and H.H.; methodology, T.H., G.W., J.L. and H.H.; software, T.H., G.W.; validation, G.W., J.L. and H.H.; formal analysis, T.H., G.W., J.L. and H.H.; investigation, T.H., G.W., J.L. and H.H.; resources, H.H.; data curation, T.H., G.W., J.L. and H.H.; writing-original draft preparation, T.H., G.W. and H.H.; writing-review

and editing, T.H., G.W., J.L. and H.H.; visualization, T.H.; supervision, G.W., J.L. and H.H.; project administration, H.H. All authors have read and agreed to the published version of the manuscript.

A Zero electric potential gauge and boundary conditions

In this Appendix, we will discuss a particular gauge choice of the boundary conditions and present a microscopic derivation of the dimensionless boundary condition $(\boldsymbol{\nabla} - \mathrm{i}\boldsymbol{A})\Psi_i \cdot \boldsymbol{n} = 0$. Firstly, we try to show that in the zero electric potential gauge, the dimensionless boundary conditions will take the form

$$\boldsymbol{\nabla}\Psi_i \cdot \boldsymbol{n} = 0, \quad \boldsymbol{A} \cdot \boldsymbol{n} = 0 \quad \text{and} \quad \boldsymbol{\nabla} \times \boldsymbol{A} = \boldsymbol{H} \tag{A.1}$$

as adopted in Eq. (8).

We start from the following gauge invariant boundary conditions between a two-band superconductor and an insulator (or vacuum)

$$(\boldsymbol{\nabla} - \mathrm{i}\boldsymbol{A})\Psi_i \cdot \boldsymbol{n} = 0, \quad \left(\frac{\partial \boldsymbol{A}}{\partial t} + \boldsymbol{\nabla}\varphi\right) \cdot \boldsymbol{n} = 0 \quad \text{and} \quad \boldsymbol{\nabla} \times \boldsymbol{A} = \boldsymbol{H}. \tag{A.2}$$

Here φ is defined as the electric potential. Given an arbitrary function χ, the gauge transformation takes the form as

$$\Psi_i \to \Psi_i e^{\mathrm{i}\chi}, \quad \boldsymbol{A} \to \boldsymbol{A} + \boldsymbol{\nabla}\chi \quad \text{and} \quad \varphi \to \varphi - \frac{\partial \chi}{\partial t}. \tag{A.3}$$

It is easy to show that the boundary conditions in Eq. (A.2) maintain the gauge invariance. Then with the zero electric potential gauge, we can get from the transformation in Eq. (A.3)

$$\frac{\partial \chi}{\partial t} = \varphi. \tag{A.4}$$

Plugging this condition into the second equation of the boundary conditions (A.2), it leads to

$$\frac{\partial \boldsymbol{A}}{\partial t} \cdot \boldsymbol{n} = 0 \tag{A.5}$$

in this new gauge. This equation can be integrated to give $\boldsymbol{A} \cdot \boldsymbol{n} = 0$, which transforms the boundary condition $(\boldsymbol{\nabla} - \mathrm{i}\boldsymbol{A})\Psi_i \cdot \boldsymbol{n} = 0$ into the form $\boldsymbol{\nabla}\Psi_i \cdot \boldsymbol{n} = 0$. Based on the analysis above, we can see that the boundary conditions in Eq. (A.1) are simply the result of a particular gauge choice.

Secondly, we would like to give a microscopic derivation of the dimensionless boundary condition $(\boldsymbol{\nabla} - \mathrm{i}\boldsymbol{A})\Psi_i \cdot \boldsymbol{n} = 0$ which is presented in Eq. (A.2). We try to show that at the interface of two-band superconductor and insulator (or vacuum), this boundary condition is applicable not only for the simple U(1)×U(1) symmetric model studied here but also the two-component GL models in general. In this process, we will follow the procedure in the single-band case suggested by de Gennes [44].

Based on the work of Zhitomirsky and Dao [45], we write the Hamiltonian of a two-band superconductor as

$$H = \sum_{i\sigma} c^{\dagger}_{i\sigma}(\boldsymbol{r})\hat{h}(\boldsymbol{r})c_{i\sigma}(\boldsymbol{r}) - \sum_{ii'} g_{ii'} c^{\dagger}_{i\uparrow}(\boldsymbol{r})c^{\dagger}_{i\downarrow}(\boldsymbol{r})c_{i'\downarrow}(\boldsymbol{r})c_{i'\uparrow}(\boldsymbol{r}). \tag{A.6}$$

Here, $i, i' = 1, 2$ are the band indices and $\sigma = \uparrow, \downarrow$ is the spin index. $\hat{h}(\boldsymbol{r})$ is the single particle Hamiltonian of the normal metal, and $g_{ii'}$ are the effective electron-electron interaction constants with $g_{12} = g_{21}$.

We can introduce the gap functions

$$\Delta_i(\boldsymbol{r}) = -\sum_{i'} g_{ii'} \left\langle c_{i'\downarrow}(\boldsymbol{r}) c_{i'\uparrow}(\boldsymbol{r}) \right\rangle \tag{A.7}$$

and transform the Hamiltonian into the mean field form

$$H_{\text{eff}} = \sum_{i\sigma} c^{\dagger}_{i\sigma}(\boldsymbol{r}) \hat{h}(\boldsymbol{r}) c_{i\sigma}(\boldsymbol{r}) + \sum_{i} \left[\Delta_i(\boldsymbol{r}) c^{\dagger}_{i\uparrow}(\boldsymbol{r}) c^{\dagger}_{i\downarrow}(\boldsymbol{r}) + \text{H.c.} \right]. \tag{A.8}$$

This effective Hamiltonian can be diagonalized by means of the Bogoliubov transformation with b and $b^{\dagger}$ the annihilation and creation operators of quasi-particle excitations

$$c_{i\uparrow}(\boldsymbol{r}) = \sum_{\boldsymbol{k}} \left[u_{i\boldsymbol{k}}(\boldsymbol{r}) b_{i\boldsymbol{k}\uparrow} - v^{*}_{i\boldsymbol{k}}(\boldsymbol{r}) b^{\dagger}_{i\boldsymbol{k}\downarrow} \right] \tag{A.9}$$

and

$$c_{i\downarrow}(\boldsymbol{r}) = \sum_{\boldsymbol{k}} \left[u_{i\boldsymbol{k}}(\boldsymbol{r}) b_{i\boldsymbol{k}\downarrow} + v^{*}_{i\boldsymbol{k}}(\boldsymbol{r}) b^{\dagger}_{i\boldsymbol{k}\uparrow} \right] \tag{A.10}$$

where $\boldsymbol{k}$ is the wave vector. With the anti-commutation relations between the fermion operators and the equation of motion for $c_{i\sigma}(\boldsymbol{r})$, we can obtain the Bogoliubov-de Gennes equations for a two-band superconductor

$$\begin{pmatrix} \hat{h} & \Delta_i(\boldsymbol{r}) \\ \Delta^{*}_i(\boldsymbol{r}) & -\hat{h}^{*} \end{pmatrix} \begin{pmatrix} u_{i\boldsymbol{k}}(\boldsymbol{r}) \\ v_{i\boldsymbol{k}}(\boldsymbol{r}) \end{pmatrix} = E_{i\boldsymbol{k}} \begin{pmatrix} u_{i\boldsymbol{k}}(\boldsymbol{r}) \\ v_{i\boldsymbol{k}}(\boldsymbol{r}) \end{pmatrix} \tag{A.11}$$

where $E_{i\boldsymbol{k}}$ is the energy of the excitation. Then with Eq. (A.7), we can transform the self-consistent gap equations into

$$\Delta_i(\boldsymbol{r}) = \sum_{i'\boldsymbol{k}} g_{ii'} v^{*}_{i'\boldsymbol{k}}(\boldsymbol{r}) u_{i'\boldsymbol{k}}(\boldsymbol{r}) \left[1 - 2f(E_{i'\boldsymbol{k}}) \right] \tag{A.12}$$

with $f\left(E_{i\boldsymbol{k}}\right) = \left[1 + \exp\left(E_{i\boldsymbol{k}}/k_B T\right)\right]^{-1}$ and T the temperature.

In the analogy with the single-band case, for small gap functions Δ_i, we can obtain the linearized form of self-consistency conditions from Eqs. (A.11) and (A.12) as

$$\Delta_i(\boldsymbol{r}) = \sum_{i'} \int K_{ii'}(\boldsymbol{r}, \boldsymbol{r}') \Delta_{i'}(\boldsymbol{r}') \mathrm{d}\boldsymbol{r}' \tag{A.13}$$

with the kernel

$$K_{ii'}(\boldsymbol{r}, \boldsymbol{r}') = \frac{g_{ii'}}{2} \sum_{\boldsymbol{k}\boldsymbol{k}'} \frac{\tanh\left(\frac{\varepsilon_{i'\boldsymbol{k}}}{2k_B T}\right) + \tanh\left(\frac{\varepsilon_{i'\boldsymbol{k}'}}{2k_B T}\right)}{\varepsilon_{i'\boldsymbol{k}} + \varepsilon_{i'\boldsymbol{k}'}} \Phi^{*}_{i'\boldsymbol{k}}\left(\boldsymbol{r}'\right) \Phi^{*}_{i'\boldsymbol{k}'}\left(\boldsymbol{r}'\right) \Phi_{i'\boldsymbol{k}}\left(\boldsymbol{r}\right) \Phi_{i'\boldsymbol{k}'}\left(\boldsymbol{r}\right). \tag{A.14}$$

Here $\Phi_{i'\boldsymbol{k}}(\boldsymbol{r})$ and $\varepsilon_{i'\boldsymbol{k}}$ are defined as the normal-state eigenfunction and eigenvalue of the electron with $\hat{h}\Phi_{i'\boldsymbol{k}} = \varepsilon_{i'\boldsymbol{k}} \Phi_{i'\boldsymbol{k}}$.

We now assume the small spatial variations in the vector potential $\boldsymbol{A}$. Then the eigenfunctions $\Phi_{i'\boldsymbol{k}}$ in the normal metal in the presence of $\boldsymbol{A}$ will differ from the eigenfunctions $w_{i'\boldsymbol{k}}$ in the absence of $\boldsymbol{A}$ by only a phase factor, i.e.,

$$\Phi^{*}_{i'\boldsymbol{k}}(\boldsymbol{r}') \Phi_{i'\boldsymbol{k}}(\boldsymbol{r}) \to w^{*}_{i'\boldsymbol{k}}(\boldsymbol{r}') w_{i'\boldsymbol{k}}(\boldsymbol{r}) \exp\left[\frac{\mathrm{i}}{2} \boldsymbol{A} \cdot (\boldsymbol{r} - \boldsymbol{r}') \right]. \tag{A.15}$$

Plugging into Eq. (A.13), it will lead to

$$\Delta_i(\boldsymbol{r}) = \sum_{i'} \int \overline{K}_{ii'}(\boldsymbol{r}, \boldsymbol{r}') \Delta_{i'}(\boldsymbol{r}') \exp\left[\mathrm{i}\boldsymbol{A} \cdot (\boldsymbol{r} - \boldsymbol{r}') \right] \mathrm{d}\boldsymbol{r}' \tag{A.16}$$

with the kernel in the absence of external magnetic field

$$\overline{K}_{ii'}(\boldsymbol{r},\boldsymbol{r}')=\frac{g_{ii'}}{2}\sum_{\boldsymbol{k}\boldsymbol{k}'}\frac{\tanh\left(\frac{\varepsilon_{i'\boldsymbol{k}}}{2k_BT}\right)+\tanh\left(\frac{\varepsilon_{i'\boldsymbol{k}'}}{2k_BT}\right)}{\varepsilon_{i'\boldsymbol{k}}+\varepsilon_{i'\boldsymbol{k}'}}w^*_{i'\boldsymbol{k}}(\boldsymbol{r}')\,w^*_{i'\boldsymbol{k}'}(\boldsymbol{r}')\,w_{i'\boldsymbol{k}}(\boldsymbol{r})w_{i'\boldsymbol{k}'}(\boldsymbol{r}). \tag{A.17}$$

Thus from Eq. (A.16), we can write

$$\Delta_i(\boldsymbol{r})=\overline{\Delta}_i(\boldsymbol{r})\exp(\mathrm{i}\boldsymbol{A}\cdot\boldsymbol{r}) \tag{A.18}$$

with $\overline{\Delta}_i(\boldsymbol{r})$ the superconducting gap function in the absence of $\boldsymbol{A}$. Then we have

$$\overline{\Delta}_i(\boldsymbol{r})=\sum_{i'}\int\overline{K}_{ii'}(\boldsymbol{r},\boldsymbol{r}')\overline{\Delta}_{i'}(\boldsymbol{r}')\mathrm{d}\boldsymbol{r}'. \tag{A.19}$$

Now, we can examine the behavior of the superconducting gap functions near the superconductor-insulator interface. Following the procedure pioneered by de Gennes, we suppose that the gap functions close to the surface behaves as

$$\overline{\Delta}_i(s)=\overline{\Delta}_{i0}+\left(\sum_{i'}\frac{\xi_1}{b_{ii'}}\overline{\Delta}_{i'0}\right)s. \tag{A.20}$$

Here s measures the normal distance from the boundary in units of ξ_1 and $s>0$ is defined in the superconductor. For simplicity, we set the cross section of the boundary as 1. $\overline{\Delta}_{i0}$ represents the gap function at the boundary and $b_{ii'}$ denotes the intraband or interband surface extrapolation length for the two-band superconductor. From Eq. (A.20), we can establish the boundary condition between the two-band superconductor and the insulator (or vacuum) at $s=0$

$$\frac{\mathrm{d}\overline{\Delta}_i}{\mathrm{d}s}=\sum_{i'}\frac{\xi_1}{b_{ii'}}\overline{\Delta}_{i'} \tag{A.21}$$

in the absence of external magnetic field.

Meanwhile, with the explicit expressions of the kernels in the bulk system and the addition of nonlinear terms to the gap equations, we can obtain the two-band GL equations from Eq. (A.19) as [45]

$$-\alpha_1\overline{\Delta}_1+\beta_1\left|\overline{\Delta}_1\right|^2\overline{\Delta}_1-\gamma_1\boldsymbol{\nabla}^2\overline{\Delta}_1-R_{12}\overline{\Delta}_2=0 \tag{A.22}$$

and

$$-\alpha_2\overline{\Delta}_2+\beta_2\left|\overline{\Delta}_2\right|^2\overline{\Delta}_2-\gamma_2\boldsymbol{\nabla}^2\overline{\Delta}_2-R_{12}\overline{\Delta}_1=0, \tag{A.23}$$

with the GL parameters

$$\alpha_{1,2}=N_{1,2}\left[\frac{1}{\lambda_{\max}}-\frac{\lambda_{22,11}}{\lambda}+\ln\left(\frac{T_{c0}}{T}\right)\right],\quad \beta_i=\frac{7\zeta(3)N_i}{16\pi^2(k_BT_{c0})^2},$$
$$\gamma_i=\frac{7\zeta(3)\hbar^2N_iv_{Fi}^2}{16\pi^2(k_BT_{c0})^2}\quad\text{and}\quad R_{12}=\frac{N_1\lambda_{12}}{\lambda}=\frac{N_2\lambda_{21}}{\lambda}. \tag{A.24}$$

Here $\lambda_{ii'}=g_{ii'}N_{i'}$ with $N_{i'}$ the density of states at the Fermi level for each band, $\lambda=\lambda_{11}\lambda_{22}-\lambda_{12}\lambda_{21}$ and $\lambda_{\max}=\frac{1}{2}\left[(\lambda_{11}+\lambda_{22})+\sqrt{(\lambda_{11}-\lambda_{22})^2+4\lambda_{12}\lambda_{21}}\right]$ the largest eigenvalue of λ-matrix. T_{c0} is the bulk critical temperature and $\boldsymbol{v}_{Fi}$ is the average Fermi velocity for each band.

In the spatially homogeneous case, we can neglect the gradient γ-terms. Eqs. (A.22) and (A.23) yield the gap equation at $T = T_{c0}$

$$\begin{pmatrix} \lambda_{11} & \lambda_{12} \\ \lambda_{21} & \lambda_{22} \end{pmatrix} \begin{pmatrix} \overline{\Delta}_1 \\ \overline{\Delta}_2 \end{pmatrix} = \lambda_{\max} \begin{pmatrix} \overline{\Delta}_1 \\ \overline{\Delta}_2 \end{pmatrix}, \tag{A.25}$$

which obviously gives the consistent result.

Now, we try to determine the coefficients $b_{ii'}$ in Eq. (A.21) by solving the linearized gap equation (A.19) in absence of external magnetic field. If we introduce $\overline{K}^0_{ii'}(s,s')$ as the kernel of gap functions in the superconducting bulk system, we can transform Eq. (A.19) into

$$\overline{\Delta}_i(s) - \sum_{i'} \int \overline{K}^0_{ii'}(s,s')\overline{\Delta}_{i'}(s')\mathrm{d}s' = -\sum_{i'} \int \left[\overline{K}^0_{ii'}(s,s') - \overline{K}_{ii'}(s,s')\right] \overline{\Delta}_{i'}(s')\mathrm{d}s' \equiv -\sum_{i'} H_{ii'}(s). \tag{A.26}$$

From Eqs. (A.22) and (A.23) with the higher order β-terms omitted, also noting that $\overline{K}^0_{ii'}(s,s') = \overline{K}^0_{ii'}(s-s')$ due to the translational symmetry, we can read out the Laplace transformation of $\overline{K}^0_{ii'}$ as

$$\overline{K}^0_{ii'}(p) = \frac{\lambda_{ii'}}{\lambda_{\max}} + \frac{\lambda_{ii'}\gamma_{i'}}{N_{i'}\xi_1^2} p^2. \tag{A.27}$$

Plugging Eq. (A.27) into (A.26), we can get

$$\overline{\Delta}_i(p) - \sum_{i'} \left(\frac{\lambda_{ii'}}{\lambda_{\max}}\right) \overline{\Delta}_{i'}(p) - \sum_{i'} \left(\frac{\lambda_{ii'}\gamma_{i'}}{N_{i'}\xi_1^2}\right) p^2 \overline{\Delta}_{i'}(p) = -\sum_{i'} H_{ii'}(p). \tag{A.28}$$

Here $\overline{\Delta}_i(p)$ and $H_{ii'}(p)$ are the Laplace transformations of $\overline{\Delta}_i(s)$ and $H_{ii'}(s)$ respectively. Since the first two terms of the left-handed side in Eq. (A.28) can be cancelled out according to Eq. (A.25), we then have

$$\sum_{i'} \left(\frac{\lambda_{ii'}\gamma_{i'}}{N_{i'}\xi_1^2}\right) p^2 \overline{\Delta}_{i'}(p) = \sum_{i'} H_{ii'}(p). \tag{A.29}$$

We can see that both sides in Eq. (A.29) take the main contribution from the boundary region.

Notice that the Laplace transformation of the gap function in Eq. (A.20) takes the form

$$\overline{\Delta}_i(p) = \frac{\overline{\Delta}_{i0}}{p} + \sum_{i'} \frac{\xi_1 \overline{\Delta}_{i'0}}{b_{ii'} p^2}. \tag{A.30}$$

Then at $p \to 0$, we will obtain from Eq. (A.29)

$$\sum_{i'i''} \left(\frac{\lambda_{ii'}\gamma_{i'}}{N_{i'}\xi_1 b_{i'i''}}\right) \overline{\Delta}_{i''0} = \sum_{i'} H_{ii'}(p=0). \tag{A.31}$$

Parallel to de Gennes' analysis, we have the sum rules

$$\int \overline{K}^0_{ii'}(s,s')\mathrm{d}s' = \frac{\lambda_{ii'}}{\lambda_{\max}} \quad \text{and} \quad \int \overline{K}_{ii'}(s,s')\mathrm{d}s' = \frac{\lambda_{ii'} N_{i'}(s)}{\lambda_{\max} N_{i'}} \tag{A.32}$$

with $N_{i'}(s)$ the local density of states at the Fermi surface. Then, we can write the Laplace transformation of the kernel difference at $p \to 0$

$$H_{ii'}(p=0) = \int H_{ii'}(s)\mathrm{d}s = \frac{\lambda_{ii'}\overline{\Delta}_{i'0}}{\lambda_{\max}} \int \frac{\overline{\Delta}_{i'}(s)}{\overline{\Delta}_{i'0}} \left[1 - \frac{N_{i'}(s)}{N_{i'}}\right] \mathrm{d}s. \tag{A.33}$$

Now we suppose $\overline{\Delta}_{i'}(s)/\overline{\Delta}_{i'0}$ approaches zero in the insulating region and is of the order of 1 in the metallic region. $N_{i'}(s)/N_{i'}$ also passes from $0 \to 1$ in a few interatomic distances from the boundary. Therefore, the integrand in Eq. (A.33) is nonvanishing only in a width of order of the lattice constant a. We can then estimate $H_{ii'}(p=0)$ as

$$H_{ii'}(p=0) = \frac{\lambda_{ii'}a}{\lambda_{\max}\xi_1}\overline{\Delta}_{i'0}. \tag{A.34}$$

Comparing Eq. (A.31) with Eq. (A.34), we can finally obtain

$$\frac{1}{b_{ii}} = \frac{N_i a}{\gamma_i \lambda_{\max}} \quad \text{and} \quad \frac{1}{b_{12}} = \frac{1}{b_{21}} = 0. \tag{A.35}$$

At this stage, we would like to point out that $1/b_{ii'} = 0$ $(i \neq i')$ is only an approximation and will become nonzero in the higher-order calculation. Even for a contact between a superconductor and an insulator, the Cooper pairs can still diffuse into the insulating region with some probability. Algebraically, this means that the gap function $\overline{\Delta}_{i'}(s)$ will also extend into the $s<0$ region, and we can roughly estimate $\overline{\Delta}_{i'}(s) \sim \sum_{i''} T_{i'i''}\overline{\Delta}_{i''0}e^{\xi_1 s/a}$ $(s<0)$ with $T_{i'i''}$ the element of the transmission matrix at the boundary. Including the $s<0$ part in the integration of Eq. (A.33) and noting $N_{i'}(s)/N_{i'} \approx 0$ in this region, we can get $H_{ii'}(p=0) = (\lambda_{ii'}a/\lambda_{\max}\xi_1)(\overline{\Delta}_{i'0} + \sum_{i''} T_{i'i''}\overline{\Delta}_{i''0})$. Plugging into Eq. (A.31), the coefficients of boundary terms are given by

$$\frac{1}{b_{ii}} = \frac{N_i a}{\gamma_i \lambda_{\max}}(1+T_{ii}), \quad \frac{1}{b_{12}} = \frac{N_1 a}{\gamma_1 \lambda_{\max}} T_{12} \quad \text{and} \quad \frac{1}{b_{21}} = \frac{N_2 a}{\gamma_2 \lambda_{\max}} T_{21}. \tag{A.36}$$

With the transmission coefficient from the superconductor to the insulator $T_{ii'} \ll 1$, we can obviously see that Eq. (A.35) is a good approximation.

For a typical two-band superconductor, we can estimate $\gamma_i \lambda_{\max}/N_i \sim \xi_1^2$ with $\xi_1 \sim 10^{-4}$ cm and the lattice constant $a \sim 10^{-8}$ cm, which will give $b_{ii} \sim 1$ cm. Therefore for a boundary separating a two-band superconductor from an insulator we can set $\xi_1/b_{ii'} \approx 0$. This leads to the boundary condition $\mathrm{d}\overline{\Delta}_i/\mathrm{d}s = 0$ from Eq. (A.21). For an arbitrary superconducting domain and in the presence of the magnetic field, we can generalize this result to $(\nabla - \mathrm{i}\mathbf{A})\Delta_i \cdot \mathbf{n} = 0$ according to Eq. (A.18). With the phenomenological superconducting order parameter $\Psi_i \propto \Delta_i$, we can finally write down the boundary condition $(\nabla - \mathrm{i}\mathbf{A})\Psi_i \cdot \mathbf{n} = 0$ for the interface of two-band superconductor and insulator.

B Discussion on convergence and relaxation time in numerical simulations

In this Appendix, we would like to justify the choice of the snapshot time at $t = 10^4 t_0$ in our numerical simulations from two perspectives. On one hand, we take the time step $\Delta t = 0.5t_0$ in our numerical calculations and treat a simulation as converged when the relative variation of the order parameter $|\Psi_1|$ between two sequential steps is smaller than 10^{-8}. Our computational results indicate that for the $15\xi_1 \times 15\xi_1$ superconducting systems with different defect configurations, the system will consistently reach the convergence before the snapshot time $10^4 t_0$. On the other hand, we can define an average velocity $\overline{v} = \sum_{\delta=1}^{W} |\boldsymbol{r}_\delta(t+\Delta t) - \boldsymbol{r}_\delta(t)|/(W\Delta t)$ for the vortices in the system, where $\boldsymbol{r}_\delta = (x_\delta, y_\delta)$ with $\delta = 1, 2, \cdots, W$ stands for the instantaneous position of each vortex core. As an example, we discuss the $15\xi_1 \times 15\xi_1$ mesoscopic sample in the presence of an isotropic impurity with the disorder strength $g = -0.5$ here. In the procedure of simulations, we notice that the vortex number in the sample will no longer change beyond $t \approx 10^3 t_0$. We then plot the variations of $\overline{v}$ with t for the vortex cluster state and the vortex lattice phase in Fig. 14. It can be seen from Fig. 14 that the $\overline{v}$ evolves with t and eventually stabilizes at $t < 10^4 t_0$. Therefore, it is justified for us to take the snapshots at $t = 10^4 t_0$ to present the stable vortex dynamics.

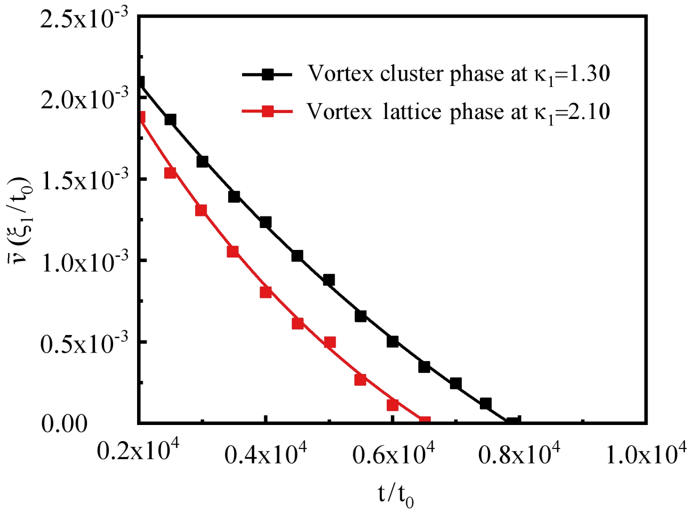

Figure 14: Variations of the average velocity $\bar{v}$ with time t at the presence of an isotropic defect with the radius $0.5\xi_1$ in the $15\xi_1 \times 15\xi_1$ type-1.5 superconductor. We set the external magnetic field $H = 0.8H_0$ in the numerical simulations.

References

[1] J. Nagamatsu, N. Nakagawa, T. Muranaka, Y. Zenitani and J. Akimitsu, *Superconductivity at 39 K in magnesium diboride*, Nature **410**, 63 (2001), doi:10.1038/35065039.

[2] M. Zehetmayer, *A review of two-band superconductivity: materials and effects on the thermodynamic and reversible mixed-state properties*, Supercond. Sci. Technol. **26**, 043001 (2013), doi:10.1088/0953-2048/26/4/043001.

[3] T. Salamone, H. G. Hugdal, S. H. Jacobsen and M. Amundsen, *High magnetic field superconductivity in a two-band superconductor*, Phys. Rev. B **107**, 174516 (2023), doi:10.1103/PhysRevB.107.174516.

[4] E. Babaev, *Vortices with fractional flux in two-gap superconductors and in extended Faddeev model*, Phys. Rev. Lett. **89**, 067001 (2002), doi:10.1103/PhysRevLett.89.067001.

[5] Y. Iguchi, R. A. Shi, K. Kihou, C. H. Lee, M. Barkman, A. L. Benfenati, V. Grinenko, E. Babaev and K. A. Moler, *Superconducting vortices carrying a temperature-dependent fraction of the flux quantum*, Science **380**, 1244 (2023), doi:10.1126/science.abp9979.

[6] Q. Z. Zhou, B. R. Chen, B. K. Xiang, I. Timoshuk, J. Garaud, Y. Li, K. Y. Liang, Q. S. He, Z. J. Li, P. H. Zhang, K. Z. Yao, H. X. Yao, E. Babaev, V. Grinenko and Y. H. Wang, *Observation of single-quantum vortex splitting in the $Ba_xK_{1-x}Fe_2As_2$ superconductor*, arXiv: 2408.05902 (2024), doi:10.48550/arXiv.2408.05902.

[7] Y. Zheng, Q. X. Hu, H. J. Ji, I. Timoshuk, H. X. Xu, Y. W. Li, Y. Gao, X. Yu, R. Wu, X. Y. Lu, V. Grinenko, E. Babaev, N. F. Q. Yuan, B. Q. Lv, C. M. Yim and H. Ding, *Direct observation of quantum vortex fractionalization in multiband superconductors*, arXiv: 2407. 18610 (2024), doi:10.48550/arXiv.2407.18610.

[8] E. Babaev and M. Speight, *Semi-Meissner state and neither type-I nor type-II superconductivity in multicomponent superconductors*, Phys. Rev. B **72**, 180502 (2005), doi:10.1103/PhysRevB.72.180502.

[9] J. Carlström, E. Babaev and M. Speight, *Type-1.5 superconductivity in multiband systems: effects of interband couplings*, Phys. Rev. B **83**, 174509 (2011), doi:10.1103/PhysRevB.83.174509.

[10] J. Carlström, J. Garaud and E. Babaev, *Length scales, collective modes, and type-1.5 regimes in three-band superconductors*, Phys. Rev. B **84**, 134518 (2011), doi:10.1103/PhysRevB.84.134518.

[11] V. Moshchalkov, M. Menghini, T. Nishio, Q. H. Chen, A. V. Silhanek, V. H. Dao, L. F. Chibotaru, N. D. Zhigadlo and J. Karpinski, *Type-1.5 superconductivity*, Phys. Rev. Lett. **102**, 117001 (2009), doi:10.1103/PhysRevLett.102.117001.

[12] C. W. Hicks, J. R. Kirtley, T. M. Lippman, N. C. Koshnick, M. E. Huber, Y. Maeno, W. M. Yuhasz, M. B. Maple and K. A. Moler, *Limits on superconductivity-related magnetization in Sr_2RuO_4 and $PrOs_4Sb_{12}$ from scanning SQUID microscopy*, Phys. Rev. B **81**, 214501 (2010), doi:10.1103/PhysRevB.81.214501.

[13] S. J. Ray, A. S. Gibbs, S. J. Bending, P. J. Curran, E. Babaev, C. Baines, A. P. Mackenzie and S. L. Lee, *Muon-spin rotation measurements of the vortex state in Sr_2RuO_4: type-1.5 superconductivity, vortex clustering, and a crossover from a triangular to a square vortex lattice*, Phys. Rev. B **89**, 094504 (2014), doi:10.1103/PhysRevB.89.094504.

[14] I. Kawasaki, I. Watanabe, H. Amitsuka, K. Kunimori, H. Tanida and Y. Onuki, *Superconducting properties of noncentrosymmetric superconductor $LaPt_3Si$ studied by muon spin spectroscopy*, J. Phys. Soc. Jpn. **82**, 084713 (2013), doi:10.7566/JPSJ.82.084713.

[15] T. Fujisawa, A. Yamaguchi, G. Motoyama, D. Kawakatsu, A. Sumiyama, T. Takeuchi, R. Settai and Y. Onuki, *Magnetization measurements of non-centrosymmetric superconductor $LaPt_3Si$: construction of low temperature magnetometers with the SQUID and Hall sensor*, Jpn. J. Appl. Phys. **54**, 048001 (2015), doi:10.7567/JJAP.54.048001.

[16] Y. S. Yerin and A. N. Omelyanchouk, *Coherent current states in a two-band superconductor*, Low Temp. Phys. **33**, 401 (2007), doi:10.1063/1.2737547.

[17] R. M. Silva, M. V. Milošević, D. Domínguez, F. M. Peeters and J. A. Aguiar, *Distinct magnetic signatures of fractional vortex configurations in multiband superconductors*, Appl. Phys. Lett. **105**, 232601 (2014), doi:10.1063/1.4904010.

[18] S. Maiti, M. Sigrist and A. Chubukov, *Spontaneous currents in a superconductor with $s+is$ symmetry*, Phys. Rev. B **91**, 161102 (2015), doi:10.1103/PhysRevB.91.161102.

[19] J. Garaud, M. Silaev and E. Babaev, *Thermoelectric signatures of time-reversal symmetry breaking states in multiband superconductors*, Phys. Rev. Lett. **116**, 097002 (2016), doi:10.1103/PhysRevLett.116.097002.

[20] V. L. Vadimov and M. A. Silaev, *Polarization of the spontaneous magnetic field and magnetic fluctuations in $s+is$ anisotropic multiband superconductors*, Phys. Rev. B **98**, 104504 (2018), doi:10.1103/PhysRevB.98.104504.

[21] E. V. Thuneberg, *Elementary pinning potential in type II superconductors near H_{c2}*, J. Low Temp. Phys. **57**, 415 (1984), doi:10.1007/BF00681201.

[22] E. V. Thuneberg, *Elementary pinning potentials in superconductors with anisotropic Fermi surface*, Cryogenics **29**, 236 (1989), doi:10.1016/0011-2275(89)90167-7.

[23] G. Blatter, M. V. Feigel'man, V. B. Geshkenbein, A. I. Larkin and V. M. Vinokur, *Vortices in high-temperature superconductors*, Rev. Mod. Phys. **66**, 1125 (1994), doi:10.1103/RevModPhys.66.1125.

[24] M. Friesen and P. Muzikar, *Microscopic theory of vortex pinning: impurity terms in the Ginzburg-Landau free energy*, Phys. Rev. B **53**, R11953 (1996), doi:10.1103/PhysRevB.53.R11953.

[25] S. Z. Lin, S. Maiti and A. Chubukov, *Distinguishing between $s+id$ and $s+is$ pairing symmetries in multiband superconductors through spontaneous magnetization pattern induced by a defect*, Phys. Rev. B **94**, 064519 (2016), doi:10.1103/PhysRevB.94.064519.

[26] J. Y. Ge, J. Gutierrez, V. N. Gladilin, J. T. Devreese and V. V. Moshchalkov, *Bound vortex dipoles generated at pinning centres by Meissner current*, Nat. Commun. **6**, 6573 (2015), doi:10.1038/ncomms7573.

[27] A. Schmid, *A time dependent Ginzburg-Landau equation and its application to the problem of resistivity in the mixed state*, Phys. Kondens. Mater. **5**, 302 (1966), doi:10.1007/BF02422669.

[28] L. P. Gor'kov and G. M. Éliashberg, *Generlization of the Ginzburg-Landau equations for non-stationaryproblems in the case of alloys with paramagnetic impurities*, Zh. Eksp. Teor. Fiz. **54**, 612 (1968), doi:10.1142/9789814317344_0003.

[29] W. C. Gonçalves, E. Sardella, V. F. Becerra, M. V. Milošević and F. M. Peeters, *Numerical solution of the time-dependent Ginzburg-Landau equations for mixed (d+s)-wave superconductors*, J. Math. Phys. **55**, 041501 (2014), doi:10.1063/1.4870874.

[30] P. A. S. Mosquera, R. M. da Silva, A. Vagov, A. A. Shanenko, T. C. E. Deluque and A. J. Albino, *Nonequilibrium interband phase textures induced by vortex splitting in two-band superconductors*, Phys. Rev. B **96**, 054517 (2017), doi:10.1103/PhysRevB.96.054517.

[31] C. A. Aguirre, M. R. Joya and J. Barba-Ortega, *On the vortex matter in a two-band superconducting meso-prism*, Physica C **585**, 1353867 (2021), doi:10.1016/j.physc.2021.1353867.

[32] S. Z. Du, Y. N. Zhong, S. W. Yao, L. Peng, T. T. Shi, L. N. Sang, X. L. Liu and J. Lin, *The dynamics of current-driven vortex in two-band superconductor with $s+d$ wave pairing*, Phys. Lett. A **443**, 128206 (2022), doi:10.1016/j.physleta.2022.128206.

[33] S. W. Yao, L. Peng, J. Lin, J. Chen, C. B. Cai and Y. Zhou, *Properties of vortex configurations in two-band mesoscopic superconductors with Josphson coupling: the Ginzburg-Landau theory*, J. Low. Temp. Phys. **202**, 329 (2021), doi:10.1007/s10909-020-02551-x.

[34] Y. G. Ryu, G. I. Mun, Y. N. Kwon, S. H. Kim and S. Hong, *Motion of magnetic vortices in type-II superconductor with randomly distributed pinning centers*, Physica C **602**, 1354125 (2022), doi:10.1016/j.physc.2022.1354125.

[35] Y. G. Ryu, J. H. Om, J. H. Kim, G. I. Ro, G. I. Mun and S. Hong, *The influence of surface defects on motion of magnetic vortices in mesoscopic type-II superconductor with randomly distributed pinning centers*, J. Supercond. Nov. Magn. **37**, 527 (2024), doi:10.1007/s10948-024-06694-w.

[36] COMSOL, Comsol multiphysics modeling guide, (2009), https://www.comsol.com.

[37] Q. Du, M. D. Gunzburger and J. S. Peterson, *Solving the Ginzburg-Landau equations by finite-element methods*, Phys. Rev. B **46**, 9027 (1992), doi:10.1103/PhysRevB.46.9027.

[38] T. S. Alstrøm, M. P. Sørensen, N. F. Pedersen and S. Madsen, *Magnetic flux lines in complex geometry type-II superconductors studied by the time dependent Ginzburg-Landau equation*, Acta. Appl. Math. **115**, 63 (2011), doi:10.1007/s10440-010-9580-8.

[39] B. Oripov and S. M. Anlage, *Time-dependent Ginzburg-Landau treatment of rf magnetic vortices in superconductors: vortex semiloops in a spatially nonuniform magnetic field*, Phys. Rev. E **101**, 033306 (2020), doi:10.1103/PhysRevE.101.033306.

[40] J. C. Li and Y. Q. Huang, *Time-domain finite element methods for Maxwell's equations in metamaterials*, Springer Heidelberg, New York, Dordrecht London, ISBN 978-3-642-33788-8 (2013), doi:10.1007/978-3-642-33789-5.

[41] J. Y. Ge, J. Gutierrez, A. Lyashchenko, V. Filipov, J. Li and V. V. Moshchalkov, *Direct visualization of vortex pattern transition in ZrB_{12} with Ginzburg-Landau parameter close to the dual point*, Phys. Rev. B **90**, 184511 (2014), doi:10.1103/PhysRevB.90.184511.

[42] M. P. Sørensen, N. F. Pedersenand and M. Ögren, *The dynamics of magnetic vortices in type II superconductors with pinning sites studied by the time dependent Ginzburg-Landau model*, Physica C **533**, 40 (2017), doi:10.1016/j.physc.2016.08.001.

[43] F. M. Izrailev, A. A. Krokhin and N. M. Makarov, *Anomalous localization in low-dimensional systems with correlated disorder*, Phys. Rep. **512**, 125 (2012), doi:10.1016/j.physrep.2011.11.002.

[44] P. G. de Gennes, *Superconductivity of metals and alloys*, Westview Press, New York, USA, ISBN 0-7382-0101-4 (1966), doi:10.1201/9780429497032.

[45] M. E. Zhitomirsky and V. H. Dao, *Ginzburg-Landau theory of vortices in a multigap superconductor*, Phys. Rev. B **69**, 054508 (2004), doi:10.1103/PhysRevB.69.054508.